Combined Photothermal and Chemotherapy to Induce Cancer Cell Damage in Spheroids Using Gold Nanostars and Gold Nanorods

Johana Charles, Enkhmaa Munkhsaikhan, Pauline Bregigeon, Théo Le Berre, Christophe Moulin, Laure Franqueville, Charlotte Rivière, Marie Frénéa-Robin, Yann Chevolot, Virginie Monnier

Particle & Particle Systems Characterization

Particle & Particle Systems Characterization
www.particle-journal.com

RESEARCH ARTICLE OPEN ACCESS

Combined Photothermal and Chemotherapy to Induce Cancer Cell Damage in Spheroids Using Gold Nanostars and Gold Nanorods

Johana Charles[1] | Enkhmaa Munkhsaikhan[1] | Pauline Bregigeon-Chanéac[2] | Théo Le Berre[2] | Christophe Moulin[3] | Laure Franqueville[2] | Charlotte Rivière[3,4] | Marie Frénéa-Robin[2] | Yann Chevolot[5] | Virginie Monnier[1]

[1]Ecole Centrale de Lyon, CNRS, INSA Lyon, CPE Lyon, INL, UMR5270, Université Claude Bernard Lyon 1, Ecully, France | [2]Ecole Centrale de Lyon, INSA Lyon, CNRS, Ampère, UMR5005, Université Claude Bernard Lyon 1, Ecully, France | [3]Univ Lyon, Institut Lumière Matière, CNRS, Université Claude Bernard Lyon 1, Villeurbanne, France | [4]Institut Convergence PLAsCAN, Centre de Cancérologie de Lyon (CRCL), INSERM U1052CNRS UMR5286, Centre Léon Bérard, Université De Lyon, Université Claude Bernard Lyon 1, Lyon, France | [5]CNRS, Ecole Centrale de Lyon, INSA Lyon, CPE Lyon, INL, UMR5270, Université Claude Bernard Lyon 1, Ecully, France

Correspondence: Virginie Monnier (virginie.monnier@ec-lyon.fr)

Received: 4 November 2025 | **Revised:** 7 March 2026 | **Accepted:** 31 March 2026

Keywords: cancer phototherapy | gold nanoparticles | photothermia | plasmon

ABSTRACT

Gold nanostars (GNS) show great potential for cancer therapy due to their photothermal effect under near-infrared excitation. Here we propose to combine photothermia with chemotherapy to make the treatment more efficient. GNS were prepared by a seeded-growth method involving silver nitrate in a 1-min process. The optimal conditions were 15 nm seeds, 3 mM of silver nitrate and a seeds to gold chloride ratio of 0.004 to obtain plasmonic resonance at 807 nm. These optimized GNS showed an increase of 4°C upon 808 nm excitation. Photothermal properties were similar to those of commercial gold nanorods (GNR) with a plasmon band centered at 813 nm. Then GNS and GNR were modified with PEG-SH molecules in order to incubate them with HT29 cancer cell spheroids prepared in hydrogel microwells. Spheroids were submitted to various treatments, in addition to incubation with GNS and GNR. They were also incubated with gemcitabine, a chemo-therapeutic agent, and irradiated at 808 nm, with the objective to combine chemotherapy with photothermal therapy. The dead/live cell evaluation after treatment was performed by fluorescence microscopy. The optimal combination of GNS, gemcitabine, and laser irradiation was found to induce the highest percentage of dead cells and a decrease of spheroids size.

1 | Introduction

Cancer is one of the leading causes of death worldwide, accounting for nearly 10 million deaths in 2022 [1]. The conventional therapeutic protocols for cancer include: i) surgery, which is efficient but only at the earliest cancer stages, ii) radiotherapy, which requires high doses if the tumor is located in deep tissues, and thus can cause damages to surrounding organs, iii) chemotherapy, whose efficiency may be limited due to a dense tumor microenvironment with a heterogeneous composition (fibroblasts, macrophages, lymphocytes, etc.) and abnormal vascular structures, making drug penetration difficult [2]. Immunotherapy can also be planned, but some cancers are known to be resistant to this approach for the same reason.

With typical dimensions on the same order of magnitude as biomolecules, nanoparticles are attractive for biomedicine. In oncology, nanoparticles are used both for diagnosis and therapy purposes. In particular, gold nanoparticles have been recognized for the past two decades as good candidates to generate a photothermal therapeutic effect [3]. This comes from their plasmonic properties and in particular, from their non-radiative relaxation causing electron–electron collisions, which lead to a rapid increase in temperature on the metal surface. Gold nanoparticles also offer the possibility to tune their extinction spectrum to the near-infrared (NIR) spectral region, which is also referred to as the first biological transparency window (700–950 nm) because the absorption and scattering of biological tissues are minimized [4]. Nanostar, nanoshell, and nanorod morphologies are among the most efficient nanostructures to induce the photothermal effect [5]. In particular, due to their sharp needles whose extremities are electromagnetic field 'hot spots', gold nanostars (GNS) show intense local electron densities leading to high photothermal conversion efficiency. In a recent study, GNS showed the highest photothermal conversion efficiency (46.2%) compared to nanospheres (21.6%) and nanorods (20.4%) [6]. It is also possible to finely tune their localized plasmon resonance in the NIR spectral region while maintaining a small nanoparticle size in the 25–75 nm range, which is not possible for nanoshells for instance for which the typical size to reach this region is over 150 nm [7]. In addition, they also exhibit interesting biological properties, such as low cytotoxicity and high cellular uptake [8]. Concerning gold nanorods (GNR), despite their lower photothermal conversion efficiency, they provide superior absorption and scattering cross-sections compared to gold nanospheres and nanoshells of the same size [9]. For instance, they heat at least 6 times faster than gold-silica nanoshell for the same gold mass [10]. Finally, like GNS, their localized surface plasmon resonance can be precisely tuned depending on their aspect ratio [11].

Despite these advantages, according to a recent review [12], clinical studies involving gold nanostructures for photothermal cancer therapy are still rare. The reason can be attributed to the complexity of the developed gold nanostructures that typically involve multiple steps for synthesis and functionalization and therefore cannot directly meet the needs of hospital settings. The most conclusive study was conducted with 150 nm gold-silica nanoshells (AuroShell nanoparticles) in 16 patients diagnosed with low- or intermediate-risk localized prostate cancer [13]. The photothermal treatment led to successful tumor ablation in 94% of the cases. However, for tumor ablation, temperature increase must be higher than 6°C and this may lead to cell necrosis. Thus, even with gold nanoparticles functionalized with targeting agents, the photothermal approach based on direct tumor ablation could also lead to unwanted side effects and to the death of surrounding healthy cells.

Mild hyperthermia requires lower temperature increase, in the 4°C–6°C range. It provides several advantages compared to ablative hyperthermia. In addition to limit the inflammatory responses and surrounding tissue damages, this approach can enhance the therapeutic synergy between photothermal treatment and other anti-cancer agents [14]. Indeed mild hyperthermia can increase both vascular, cell membrane, and extracellular matrix permeability, allowing for a better penetration of drugs [15]. This effect has already been investigated in several preclinical studies involving gold nanoparticles. For instance, gold nanorods were used to deliver gene editing proteins that reduce the thermal resistance of cancer cells, allowing mild hyperthermia to induce tumor apoptosis without causing deleterious effects on surrounding tissues in mice model [16]. Gold nanorods were also combined with si-RNA in order to down-regulate the heat shock protein expression and enhance apoptosis in tumor xenografts model [17]. In another example, the mild hyperthermia properties of gold nanocages coupled to hyaluronic acid were employed to increase the vascular permeability of tumor tissues in order to facilitate the deep penetration of immune cells and immunotherapeutic agents [18].

In our work, we aim to improve the efficacy of a chemotherapy drug, gemcitabine, through mild hyperthermia. Gemcitabine was selected among other chemotherapeutic agents because it is a widely used anticancer drug with demonstrated activity against a broad spectrum of solid tumors [19, 20], including colorectal cancer [21]. However, its clinical efficacy is limited by several pharmokinetic drawbacks, including poor tumor delivery and a short plasma half-life resulting from rapid enzymatic degradation [22]. We expect that hyperthermia in combination to gemcitabine could facilitate the accessibility of the drug to the tumor and reduce its toxicity by decreasing the administered dose. A previous paper reports a similar approach involving liposomal nanocarriers containing gemcitabine in combination with PEGylated gold nanorods [23]. The mild hyperthermia generated by gold nanorods led to an increased intratumor gemcitabine concentration, and a reduction of pancreatic tumor size in mice.

In the present study, we propose to compare two different gold nanostructures that were selected to reach a plasmon band in the NIR spectral region (around 800 nm): gold nanostars (GNS) and gold nanorods (GNR). In particular, GNS present a very simple synthesis protocol (in a 1 min process) and both GNS and GNR can be easily functionalized with polyethylene(glycol) to make them biocompatible. After optimization of GNS synthesis conditions, their photothermal properties were compared to those of GNR. They were both chemically modified with a thiol-terminated polyethylene(glycol) and finally incubated with multi-cellular 3D HT29 cell spheroids to mimic the interaction between gold nanoparticles and tumors in the presence of gemcitabine, and of NIR light irradiation to induce mild hyperthermia. The efficiency of this combined treatment was evaluated by fluorescence microscopy after labelling of dead cells and living cells.

2 | Experimental Section

A detailed list of materials and methods is given in the Supporting Information. Briefly, GNS were synthesized using a surfactant-free protocol [24] consisting first in the synthesis of spherical gold nanoparticles that are used as seeds for the growth of GNS branches in the presence of ascorbic acid and silver nitrate, as a shape-directing agent and catalyzer to induce branching onto gold nanoparticle active sites. The whole scheme of the synthesis process is given in Figure S1. GNR were obtained from NanoPartz company (Loveland, USA) at a gold concentration of 42 mg/L.

3 | Results and Discussion

3.1 | Optimization of the Synthesis of Surfactant-Free GNS

The surfactant-free gold nanostars synthesis protocol was optimized to obtain GNS with a plasmon band located around 800 nm, in order to match the first biological transparency window and the laser wavelength used for photothermal irradiation. The studied parameters were the size and the quantity of gold seeds as well as the quantity of added silver counter-ions. Two gold seeds diameters, 2 and 15 nm were prepared (Figure S2) and used for the synthesis of GNS starting from fixed quantities of $AgNO_3$ (3 mM, 100 µL), ascorbic acid (100 mM, 50 µL), and $HAuCl_4$ (0.25 mM, 10 mL). The extinction spectra of the obtained GNS compared to the extinction spectra of initial gold seeds of 2 and 15 nm are displayed in Figures S3a,b, respectively. For both seed diameters, a redshift of the plasmon band is observed by UV–vis absorption spectroscopy, which is consistent with a change in size or morphology of gold seeds. A larger redshift is obtained for GNS synthesized from 15 nm seeds from 520 to 702 nm, with the possibility to extend the plasmon band toward the NIR region. Thus, this seed diameter was selected for the following optimization studies. Silver ions allowed the formation of nucleation sites for the growth of gold branches around seeds. Their quantity is directly related to the number and thickness of gold branches [25]. However, as shown in previous studies, when the quantity of dissolved Au^{3+} is too low compared to the seeds quantity, GNS branches are short for any $AgNO_3$ concentration [24]. Consequently, to increase the NIR shift of GNS plasmon band, the molar ratio between gold seeds and $HAuCl_4$, defined as AuSeeds : $HAuCl_4$, was optimized. This ratio was varied from 0.001 to 0.1 using 15 nm gold seeds and a $AgNO_3$ concentration of 3 mM. An increase in the seeds to $HAuCl_4$ molar ratio leads to a blueshift of the GNS plasmon band (Figure S4). The relation between this ratio and the plasmon band maximum can be fitted by a linear curve (Figure S4b). Thus, this parameter seems to be the most relevant to precisely monitor the plasmonic properties of GNS. This effect could be explained by the growth of longer branches around gold seeds when the seeds amount decreases. Hydrodynamic diameters and zeta potential values of GNS grown for these different AuSeeds to $HAuCl_4$ molar ratios are presented in Table S1. Although zeta potential values are similar (around −30 mV) for every GNS, hydrodynamic diameters are directly correlated to the plasmon band evolution, as an increase of diameter is observed when the plasmon band is redshifted toward the infrared region. This finding is in agreement with the increase of nanostar branches length [24]. Additionally, a AuSeeds : $HAuCl_4$ molar ratio of 0.004 allows obtaining GNS with a plasmon band at 807 nm (Figure 1a) and a hydrodynamic diameter of 128 ± 1 nm, as measured by Dynamic Light Scattering (DLS). Their diameter was also measured by Transmission Electron Microscpopy (TEM) as shown in Figure 1b,c.

As expected, the observed GNS have a nanostar morphology. Their diameter was measured according to the procedure detailed in Figure S5. An average diameter of 172 ± 35 nm was measured over 100 GNS, which is higher than the measured hydrodynamic diameter. This result might be surprising as hydrodynamic diameter is generally higher than TEM-measured diameter due to the fact that DLS takes into account the solvating sphere around nanoparticles, but it may be explained by the anisotropic shape of GNS. Indeed, DLS is based on nanoparticles Brownian motion, thus the measured diameter is equal to the one of an equivalent sphere with some translational diffusion coefficient [26]. As shown in Figure 1b, some GNS cannot be assimilated to a sphere as the lengths of their branches are very heterogeneous. Additionally, in agreement with the DLS measurement, no aggregates were observed on TEM images. The gold concentration in the as-synthesized GNS was 26.3 mg/L as measured by ICP-AES.

3.2 | Initial GNR

Commercial GNR used in this study had a diameter of 13 ± 1 nm and a length of 49 ± 6 nm (measured by TEM) and were initially coated with cetyltrimethylammonium bromide (CTAB). Their plasmon band is centered at 813 nm (Figure 2a). TEM image and corresponding histogram are shown in Figure 2b,c, respectively.

3.3 | Photothermal Properties of GNS and GNR

GNS and GNR dispersions were irradiated with an 808 nm continuous wave laser and the temperature increase was followed with an IR-thermographic camera (Figure 3).

After 30 min, a temperature increment of around 4°C was observed for both GNS and GNR making them suitable to generate apoptosis without necrosis, in the 'mild hyperthermia range'. As a comparison, water irradiated under the same condition had a temperature increase smaller than 1°C. From these temperature curves, the specific absorption rate (SAR), i.e. the power dissipated per mass unit of gold, and the light-to-heat conversion efficiency can be determined [27]. Calculation details are provided in Supporting Information. The obtained values are given in Table 1.

The SAR values obtained are of the same order of magnitude than those found in the literature under mild hyperthermia. For instance, Jung et al. [28] measured the photothermal properties of GNR in similar conditions (laser power per surface unit of 60 mW/cm^2, GNR concentration of 48 mg/L) and obtained a temperature increase of 3.8 K after 10 min of laser irradiation. The SAR value calculated from this measurement is equal to 551 W g^{-1}, a value close to the 408 W g^{-1} obtained here for GNR. In comparison, SAR values up to 10000 W g^{-1} for GNS [29] and 24600 W g^{-1} for GNR [30] were found in previous studies, but in those cases, the laser power per surface unit was of 1 W/cm^2 and 0.8 W/cm^2, with temperature increase greater than 45 K in 20 min and 20 K in 16 min, respectively. These conditions are characteristic of the ablative hyperthermia regime. The low SAR values obtained in our work can be attributed to the low temperature increase of a few K measured with GNS and GNR in our mild hyperthermia conditions. However, light-to-heat conversion efficiency reached high values, particularly for GNS with almost 100%. The higher value found for GNS is supported by the work of Wang et al. [6] in which a more than

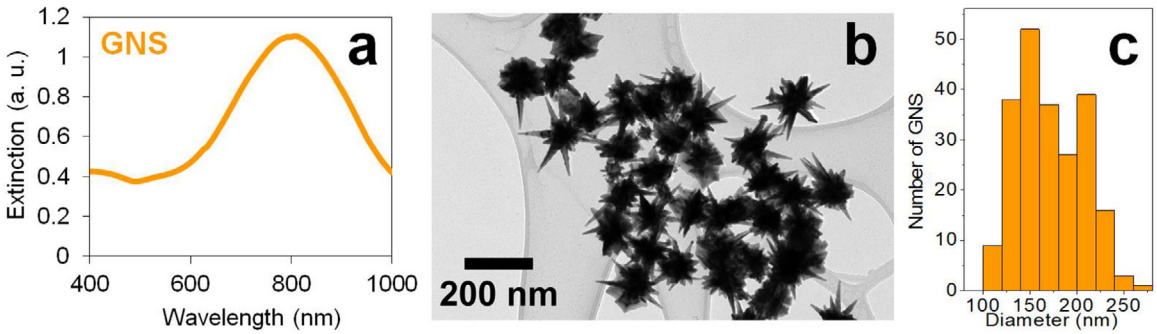

FIGURE 1 | (a) Extinction spectrum, (b) TEM image, and (c) corresponding diameter histogram of GNS prepared from a AuSeeds : $HAuCl_4$ molar ratio of 0.004, the other synthesis conditions were : initial gold seeds of 15 nm in diameter and $[AgNO_3] = 3$ mM.

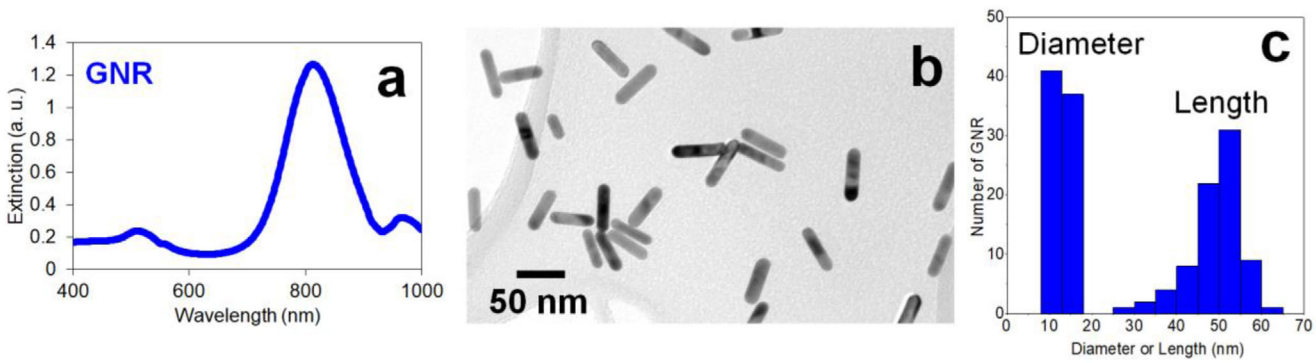

FIGURE 2 | (a) Extinction spectrum, (b) TEM image and (c) corresponding diameter and length histograms of commercial GNR.

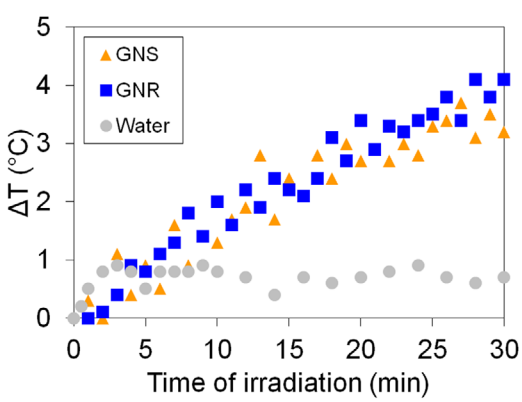

FIGURE 3 | Temperature variation (ΔT) as a function of time for GNS (orange triangles), GNR (blue squares), and water (grey circles) under irradiation with the 808 nm continuous wave laser.

twice higher photothermal conversion efficiency was found for GNS compared to GNR.

3.4 | Functionalization of GNS and GNR With PEG-SH

As GNS were synthesized with a surfactant-free procedure, they were initially uncoated and thus a thiol-terminated polyethylene(glyco) (O-[2-(3-mercaptopropionylamino)ethyl]-O′-methylpolyethylene glycol), noted PEG-SH, was added right after the end of the synthesis. Zeta potential increases from −31 ± 1 mV to −27 ± 1 mV after PEG-SH coating. The negative charge observed before PEG coating could be explained by the excess of some sodium citrate molecules on starting gold seeds. Then the increase of zeta potential value after PEG-SH coating could be explained by the replacement of sodium citrate by non-charged PEG-SH. As shown in Figure S6a, a slight blueshift was evidenced after PEG coating due to a change in the local refractive index around GNS, which is consistent with the formation of the PEG-SH layer. In addition, a 30% decrease in extinction intensity was also observed probably due to GNS losses. For GNR, they were initially coated with CTAB, which is known to be highly toxic for cells [31]. Therefore, the functionalization with PEG required first the removal of excess CTAB by centrifugation, then the addition of sodium borohydride to reduce any residual gold salts in the solution in order to prevent nanorods aggregation [32]. A decrease in zeta potential value from 45 ± 1 mV to 24 ± 1 mV was noticed, in agreement with the replacement of CTAB by PEG-SH. Similarly to GNS, a blueshift and a 52% intensity decrease were observed after PEG-SH functionalization as shown in Figure S6b. PEG-SH coating onto GNS and GNR was also confirmed by infrared spectroscopy (Figure S7). The PEG-SH spectrum shows typical stretching vibration peaks of C═O and C—O bonds in the 1000–1400 cm^{-1} range, in addition to N—H and N—C═O (amide) bending vibration peaks at 1470 and 840 cm^{-1}, respectively. The main peaks obtained in this region can be also found on GNS@PEG and GNR@PEG spectra,

TABLE 1 | SAR and light-to-heat conversion efficiency calculated for GNS and GNR.

Sample	SAR ($W.g^{-1}$)	Light-to-heat conversion efficiency (%)
GNS	350	99
GNR	408	68

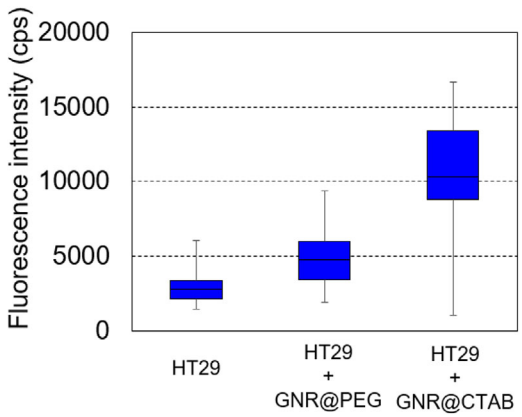

FIGURE 4 | Fluorescence intensity of IP (label of dead cells) obtained for HT29 spheroids in cell medium, treated with PEG-coated GNR and treated with CTAB-coated GNR (initial GNR).

with the C—H stretching vibration peak in the 2800–3000 cm^{-1} range. On the contrary, the GNS spectrum does not present any significant vibration peak while the GNR spectrum only shows vibration peaks corresponding to CTAB, i.e. C—H stretching vibration peak at 2800–2900 cm^{-1} and C—N stretching vibration peak at 915 cm^{-1} [32]. A zoom was made on the 800–1000 cm^{-1} spectral region (Figure S8). The spectrum of initial GNR (Figure S8d) shows only one peak at 915 cm^{-1} corresponding to C—N stretching vibration, whereas the spectra of PEG-SH (Figure S8a) and PEG-SH coated GNR (Figure S8e) present similar profiles, with peaks around 840 and 960 cm^{-1} corresponding to N—C═O (amide) bending vibration and C—O—C symmetrical stretching vibration, respectively [33]. It is clearly noticeable that the peak at 915 cm^{-1} is absent from the spectrum of PEG-SH coated GNR, proving that CTAB was not detectable anymore by infrared spectroscopy. The biocompatibility of PEG-coated GNR was then evaluated in the presence of HT29 spheroids and compared to the one of initial GNR (Figure 4).

The fluorescence intensity coming from dead cells is significantly higher for initial CTAB-coated GNR while PEG-coated GNR had a moderate increase in fluorescence compared to HT29 spheroids alone, suggesting that the PEG-SH functionalization may reduce the cytotoxicity of GNR.

3.5 | Incubation of GNS and GNR With Spheroids and Therapeutic Effect

GNS and GNR were finally incubated with HT29 spheroids in presence/absence of NIR light and/or gemcitabine to evaluate the efficiency of combined photothermal therapy and chemotherapy. Spheroids were chosen over conventional 2D cell cultures because their 3D structure better mimics patient tumors in terms of cellular layer organization, cell-to-cell communication, and spatial variation in nutrients and oxygen supply depending on the position of the cells within the tumor [34]. The HT29 cell line was selected due to its known resistance to anticancer therapies, making it a relevant model for evaluating treatment efficacy [35]. In addition, HT29 cells readily form compact and structured spheroids, with homogenous size and high reproducibility [36]. Finally, these cells exhibit rapid growth, with spheroids occupying approximately 80% of the 200 µm microwells withing 3 days of culture, thereby enabling timely and reliable evaluation of therapeutic responses. Living cells were label with fluorescein diacetate (FDA, green signal) and dead cells with IP (propidium iodide, red signal), as shown in Figure 5.

As expected HT29 spheroids without any treatment (Figure 5a) were exclusively composed of living cells. Laser irradiation for 20 min did not lead to the death of cells as shown in Figure 5b. The introduction of gemcitabine, the chemotherapeutic agent, was associated with the apparition of dead cells mainly located at the surface of spheroids (Figure 5c) without a noticeable effect of the laser (Figure 5d), as expected in the absence of gold nanoparticles. When GNS were added to HT29, the presence of dead cells was more obvious (Figure 5e) but no additional cell death was observed in the presence of laser irradiation (Figure 5f). The simultaneous addition of GNS and gemcitabine was associated to approximately the same amount of dead cells, but still located on the surface of spheroids (Figure 5g), while under laser irradiation almost 50% of the spheroids were totally composed of dead cells in their volume as shown in Figure 5h. GNR addition onto spheroids produced similar effects, whereas contrary to GNS they did not produce the death of cells without (Figure 5i) or with laser irradiation (Figure 5j). The lower toxicity of GNR compared to GNS when the laser is turned off could be attributed to the purification steps achieved to perform the PEG-SH functionalization procedure. Finally, in the presence of gemcitabine and GNR, some dead cells could be seen on the surface of spheroids (Figure 5k) while under laser irradiation, similarly to GNS, spheroids fully composed of dead cells were observed but to a lesser extent, only for 8% of the spheroids (Figure 5l). A statistical analysis was then performed on 50–200 spheroids to evaluate the fluorescence intensity emitted by dead cells in each condition. Results are displayed in Figure 6.

As shown in Figure 6, HT29 spheroids were affected by laser irradiation, the presence of gemcitabine, and GNS/GNR. In particular, the combination of gemcitabine addition and laser irradiation led to a high dispersion of the IP fluorescence values. However, for HT29 spheroids non-treated with GNS or GNR, the difference between HT29 alone and HT29 treated with gemcitabine and laser was not significant. Concerning GNS, the average intensity emitted by dead cells was higher when GNS, gemcitabine, and laser irradiation were present simultaneously. In addition, the difference between HT29 with only GNS and

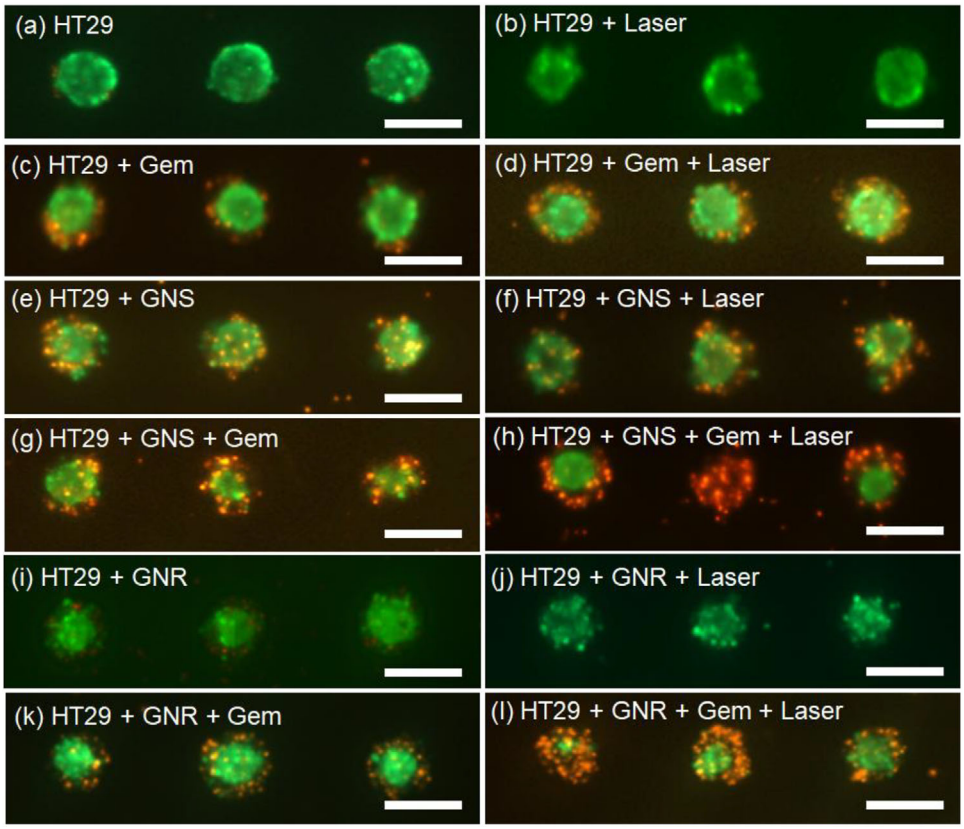

FIGURE 5 | Typical fluorescence images taken on 3 spheroids under different incubation conditions, without (a,c,e,g,i,k) or with laser irradiation at 808 nm during 20 min (b,d,f,h,j,l), in absence (a,b,e,f,i,j) or in presence of gemcitabine 10 nM (c,d,g,h,k,l) and in absence (a–d) or in presence of GNS (e–h) or GNR (i–l) at 7.8 μg/mL. Living cells were label with FDA (green signal, excitation at 488 nm) and dead cells with IP (red signal, excitation at 535 nm). All scale bars represent a distance of 200 μm.

HT29 with GNS, gemcitabine, and laser irradiation was found to be significant with a p value lower than 0.00005 in the Student's t test. The effect of the laser irradiation was also significant with a p value lower than 0.0005 for HT29 with GNS and gemcitabine compared to HT29 with GNS, gemcitabine, and laser irradiation. For GNR, the average intensity was similar for spheroids in the presence of GNR and gemcitabine without or with laser irradiation. However, the intensity values were significantly more dispersed, with very intense values leading to a large standard deviation. Nevertheless, the combination of GNR, gemcitabine, and laser irradiation seems to be to some extent effective thanks to the photothermal effect and chemotherapy compared to HT29 with GNR, with a p value below 0.00005. However, for GNR, the benefit of laser irradiation was not significant when comparing HT29 with GNR and gemcitabine, and HT29 with GNR, gemcitabine, and laser irradiation. The dual photothermal-chemotherapeutic effect was also evidenced by its impact on spheroid size. This was evaluated by measuring the average area of living cells (FDA label) in each spheroid (Figure 7).

As expected, non-treated HT29 spheroids have the highest area covered by living cells, proving their healthy nature (Figure 7). All the treatments have a significant impact on their area and thus on the size of spheroids. The following treatments, i.e. laser, gemcitabine, gemcitabine + laser, GNS, GNS + laser, GNS + gemcitabine, GNR, and GNR + laser show comparable effects, with a decrease by approximately 30% in size compared to the non-treated spheroids. However, the combined therapy (laser + gemcitabine) on GNS produces a higher effect with a decrease of around 50% in size compared to the non-treated spheroids. Although this was also observed with GNR in combination with gemcitabine, the beneficial effect of the laser was not significant. To better assess the influence of the different treatments on spheroids size, the equivalent diameter of spheroids was calculated from the projected area and then from this equivalent diameter, the equivalent volume of spheroids was also evaluated (Figure 8).

As shown in Figure 8, equivalent diameter and volume of spheroids follow the same trend as the projected area. Given that a HT29 single cell has an average size of 10–15 μm, the decrease in diameter obtained for HT29 spheroids after laser, gemcitabine gemcitabine + laser treatments can be attributed to the removal of 1 cell layer in spheroids. Similar effects were obtained after addition of GNS, GNS + laser, GNS + gemcitabine, GNR, and GNR + laser. However, GNS + gemcitabine + laser, GNR + gemcitabine, and GNR + gemcitabine + laser induced a larger decrease in diameter, that can assigned to the removal of 2 cell layers in spheroids. Differences obtained for equivalent volumes are even more significant with almost 70% of spheroids volume decrease after GNS + gemcitabine + laser, GNR + gemcitabine, and GNR + gemcitabine + laser treatments compared to non-treated HT29 spheroids.

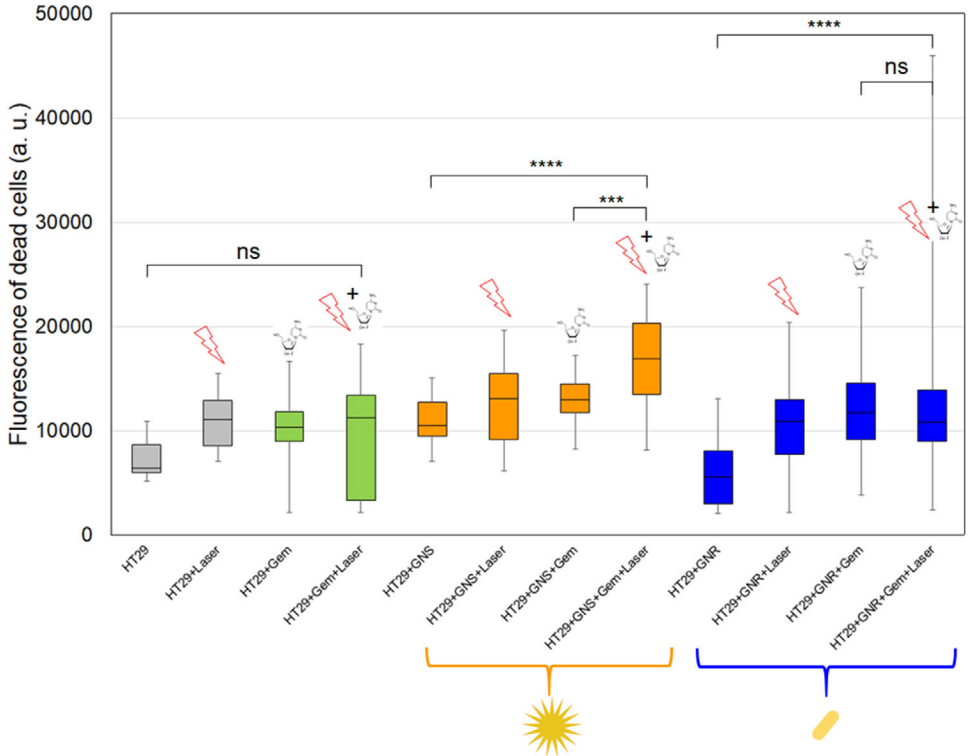

FIGURE 6 | IP fluorescence intensity (label of dead cells) obtained for 1) non treated HT29 spheroids, 2) HT29 treated by 808 nm laser, 3) by gemcitabine, 4) in presence of gemcitabine and treated by 808 nm laser, 5) in presence of GNS, 6) in presence of GNS and treated by 808 nm laser, 7) in presence of GNS + gemcitabine, 8) in presence of GNS + gemcitabine and treated by 808 nm laser, 9) in presence of GNR, 10) in presence of GNR and treated by 808 nm laser, 11) in presence of GNR + gemcitabine, 12) in presence of GNR + gemcitabine and treated by 808 nm laser. Student's *t* test: ****: $p < 0.00005$, ***: $p < 0.0005$, ns : non significant.

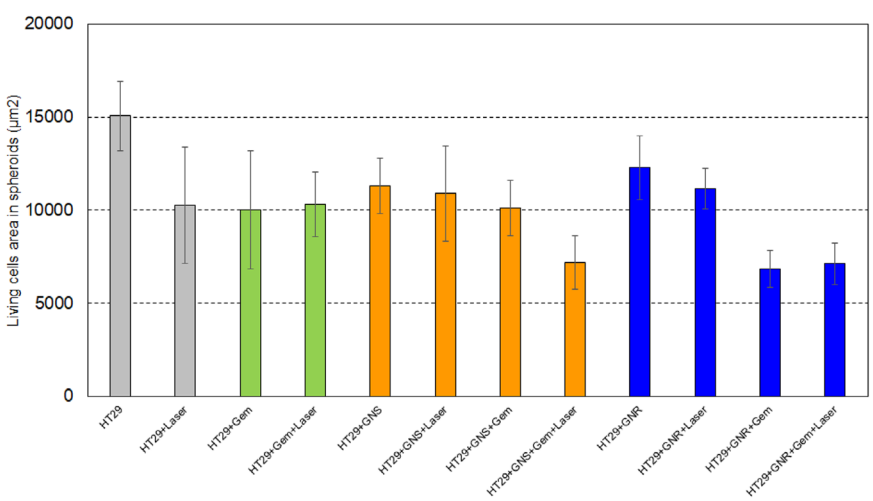

FIGURE 7 | Average projected area of living cells (FDA label) by spheroid at day 6 of growth for 1) non treated HT29 spheroids, 2) HT29 treated by 808 nm laser, 3) by gemcitabine, 4) in presence of gemcitabine and treated by 808 nm laser, 5) in presence of GNS, 6) in presence of GNS and treated by 808 nm laser, 7) in presence of GNS + gemcitabine, 8) in presence of GNS + gemcitabine and treated by 808 nm laser, 9) in presence of GNR, 10) in presence of GNR and treated by 808 nm laser, 11) in presence of GNR + gemcitabine, 12) in presence of GNR + gemcitabine and treated by 808 nm laser.

According to these results, it seems that GNS outperform GNR for combined chemotherapy/photothermal therapy. The multiple sharp spikes exhibited by GNS can be considered as plasmonic 'hot spots' on which there is a very intense local electromagnetic field. It leads to an enhanced heat generation per particle which is supported by the higher light-to-heat conversion efficiency found for GNS compared to GNR as shown in Table 1 and in a previous work [6]. Due to their bigger size, it is also associated to a higher

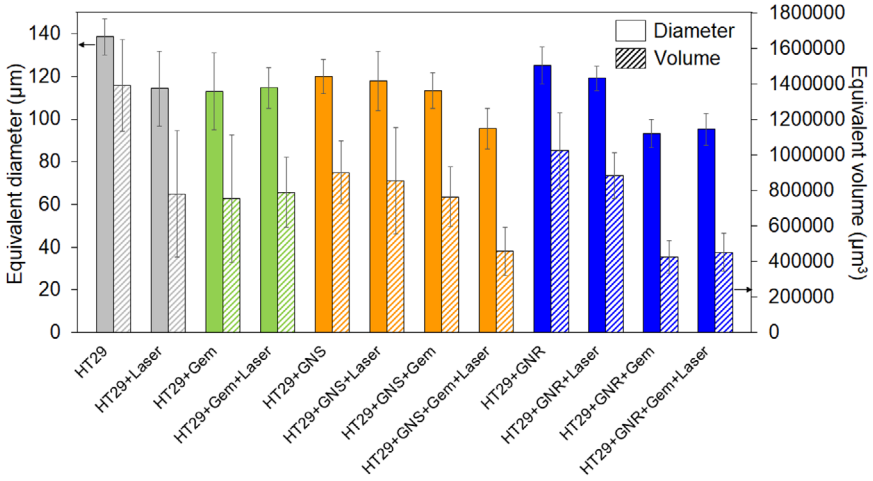

FIGURE 8 | Average equivalent diameter (left axis, non-hatched bars) and average equivalent volume (right axis, hatched bars) of spheroids calculated from the average projected area of living cells at day 6 of growth for 1) non treated HT29 spheroids, 2) HT29 treated by 808 nm laser, 3) by gemcitabine, 4) in presence of gemcitabine and treated by 808 nm laser, 5) in presence of GNS, 6) in presence of GNS and treated by 808 nm laser, 7) in presence of GNS + gemcitabine, 8) in presence of GNS + gemcitabine and treated by 808 nm laser, 9) in presence of GNR, 10) in presence of GNR and treated by 808 nm laser, 11) in presence of GNR + gemcitabine, 12) in presence of GNR + gemcitabine and treated by 808 nm laser.

absorption cross-section for GNS [37]. These optical and thermal properties have important consequences on tumor penetration. In particular, Lopez-Mendez et al. have recently shown that these properties improve the interaction with spheroids [7]. Using a correlation between nanoscale thermal imaging based on x-ray absorption spectroscopy and TEM to precisely localize GNS into spheroids, they show that the photothermal effect of GNS disrupts actin cell cytoskeleton and influences cellular adhesion into the spheroids. The GNS roughness may also promote their interaction with the cell membrane and their diameter above 100 nm may favour tumor retention [38]. On the contrary, it was recently shown that PEG-coated GNR exhibit low penetration into spheroids, with an accumulation in the outer cell layers [39]. Therefore, these different behaviours in presence of spheroids may lead to a greater chemo-sensitization induced by GNS compared to GNR when photothermal therapy is combined to chemotherapy.

This preliminary study offers interesting perspectives in the field of cancer treatment to allow an improved action of chemotherapeutic drugs using phototherapy particularly when chemotherapy is lacking in efficiency, for example, in the presence of a dense tumor micro-environment. Prior to clinical translation, many important questions are still pending. The first one is to understand the in vivo fate of gold nanoparticles, i.e. their blood circulation time, their biodistribution into organs and finally their excretion. In particular, large gold nanoparticles, such as GNS, exhibit an increased internalization into solid tumors as a result from enhanced permeability and retention (EPR) effect [40]. However, they are also accumulating in liver and spleen [41], where they are mainly taken up by phagocytose. As done in our study, PEGylation can improve this, as well as increase blood circulation time [42], although it is now debated with the identification of anti-PEG antibodies, leading to immune reactions, which alter pharmacokinetics [43]. The second important issue to address is the long-term toxicity of gold nanoparticles, as a consequence of their slow elimination and their poor biodegradability. The scale-up of nanoparticles synthesis will also be a necessary step to obtain reproducible results during in vivo studies. In this case, the simplicity of our nanoformulations, particularly for GNS, which are produced in a 1-min synthesis process, will be a strong advantage. Finally, the NIR laser penetration depth into biological tissues is limited to few centimeters. To reach the tumor, an endoscope equipped with an optical fiber could be used, in addition to the delivery of gold nanoparticles by an injection channel inserted in the device.

4 | Conclusion

In summary, GNS were prepared using a surfactant-free method. The synthesis parameters were optimized to reach a plasmon band around 800 nm. Their photothermal properties under 808 nm laser excitation were found to be close to those of GNR with similar plasmonic properties, but a higher light-to-heat conversion efficiency was calculated for GNS. In addition, the absence of surfactant on their surface allowed easy functionalization with PEG-SH molecules and avoided ligand exchange steps to reduce prior toxicity, contrary to GNR. They were then incubated with HT29 cells spheroids mimicking 3D tumors, which were submitted to a combined treatment involving phototherapy under 808 nm light excitation and chemotherapy with gemcitabine. The combined therapy led to a noticeable presence of dead cells in the total volume of spheroids, with a significant decrease in the spheroids' size, in particular for GNS. Although these results are encouraging, it should be emphasized that our work represents a preliminary study with several stages remaining to be addressed before potential clinical translation. Future studies will investigate pancreatic tumor models, combining pancreatic cancer cells with tumor-associated stomal and immune cells to challenge our approach in a dense and more complex microenvironment. Subsequently, more complex 3D cellular structures, such as organoids, will be explored to better recapitulate in vivo conditions.

Acknowledgements

The authors are indebted to the institute Carnot Ingénierie@Lyon for its support and funding (Carnot 2021- IMPULSE). The research internships of J. Charles and E. Munkhsaikhan were supported by the Labex iMUST and the Graduate School of Medical Device Engineering, respectively. N. Blanchard from CLYM platform is thanked for his help with TEM experiments. T. Géhin and L. Berguiga are acknowledged for their implementation of the photothermal experiment set-up. The Nanolyon technological platform is acknowledged for its technical support.

Open access publication funding provided by COUPERIN CY26.

Conflicts of Interest

The authors declare no conflicts of interest.

Data Availability Statement

The data that support the findings of this study are available from the corresponding author upon reasonable request.

References

1. "Data visualization tools for exploring the global cancer burden in 2022, (International Agency for Research on Cancer, World Health Organization (WHO), 2022)," can be found under https://gco.iarc.fr/today/en.

2. A. N. Hosein, R. A. Brekken, and A. Maitra, "Pancreatic Cancer Stroma: An Update on Therapeutic Targeting Strategies," *Nature Reviews Gastroenterology & Hepatology* 17 (2020): 487–505, https://doi.org/10.1038/s41575-020-0300-1.

3. J. A. Webb and R. Bardhan, "Emerging Advances in Nanomedicine With Engineered Gold Nanostructures," *Nanoscale* 6 (2014): 2502–2530, https://doi.org/10.1039/c3nr05112a.

4. L. Bonacina, "Nonlinear Nanomedecine: Harmonic Nanoparticles Toward Targeted Diagnosis and Therapy," *Molecular Pharmaceutics* 10 (2013): 783–792, https://doi.org/10.1021/mp300523e.

5. J. R. Cole, N. A. Mirin, M. W. Knight, G. P. Goodrich, and N. J. Halas, "Photothermal Efficiencies of Nanoshells and Nanorods for Clinical Therapeutic Applications," *The Journal of Physical Chemistry C* 113 (2009): 12090–12094, https://doi.org/10.1021/jp9003592.

6. W. Yang, B. Xia, L. Wang, et al., "Shape Effects of Gold Nanoparticles in Photothermal Cancer Therapy," *Materials Today Sustainability* 13 (2021): 100078.

7. R. López-Méndez, A. Dubrova, J. Reguera, et al., "Multiscale Thermal Analysis of Gold Nanostars in 3D Tumor Spheroids: Integrating Cellular-Level Photothermal Effects and Nanothermometry via X-Ray Spectroscopy (Adv. Healthcare Mater. 11/2025)," *Advanced Healthcare Materials* 14 (2025): 2403799.

8. B. J. Delgado-Corrales, V. Chopra, and G. Chauhan, "Gold Nanostars and Nanourchins for Enhanced Photothermal Therapy, Bioimaging, and Theranostics," *Journal of Materials Chemistry B* 13 (2025): 399–428, https://doi.org/10.1039/D4TB01420K.

9. P. K. Jain, K. S. Lee, I. H. El-Sayed, and M. A. El-Sayed, "Calculated Absorption and Scattering Properties of Gold Nanoparticles of Different Size, Shape, and Composition: Applications in Biological Imaging and Biomedicine," *The Journal of Physical Chemistry B* 110 (2006): 7238–7248, https://doi.org/10.1021/jp057170o.

10. G. Von Maltzahn, J.-H. Park, A. Agrawal, et al., "Computationally Guided Photothermal Tumor Therapy Using Long-Circulating Gold Nanorod Antennas," *Cancer Research* 69 (2009): 3892–3900.

11. J. Zhu, N. Ouyang, R. Zhao, et al., "Black Phosphorus Nanosheets Grafted With Gold Nanorods and Carbon Nanodots for Synergistic Antitumor Therapy," *ACS Applied Materials & Interfaces* 15 (2023): 26241–26251, https://doi.org/10.1021/acsami.3c00524.

12. R. Zhang, F. Kiessling, T. Lammers, and R. M. Pallares, "Clinical Translation of Gold Nanoparticles," *Drug Delivery and Translational Research* 13 (2023): 378–385, https://doi.org/10.1007/s13346-022-01232-4.

13. A. R. Rastinehad, H. Anastos, E. Wajswol, et al., "Gold Nanoshell-Localized Photothermal Ablation of Prostate Tumors in a Clinical Pilot Device Study," *Proceedings of the National Academy of Sciences* 116 (2019): 18590–18596.

14. M. N. Amaral, P. Kumar, P. Faísca, et al., "Gold Nanoparticle-Mediated Photothermal Therapy: Expanding the Frontiers of Cancer Treatment and Theragnostics," *Biomedicine & Pharmacotherapy* 190 (2025): 118399, https://doi.org/10.1016/j.biopha.2025.118399.

15. R. S. Riley and E. S. Day, "Gold Nanoparticle-Mediated Photothermal Therapy: Applications and Opportunities for Multimodal Cancer Treatment," *Wiley Interdisciplinary Reviews: Nanomedicine and Nanobiotechnology* 9 (2017): 1449.

16. X. Li, Y. Pan, C. Chen, et al., "Hypoxia-Responsive Gene Editing to Reduce Tumor Thermal Tolerance for Mild-Photothermal Therapy," *Angewandte Chemie International Edition* 60 (2021): 21200–21204, https://doi.org/10.1002/anie.202107036.

17. B.-K. Wang, X.-F. Yu, J.-H. Wang, et al., "Gold-Nanorods-siRNA Nanoplex for Improved Photothermal Therapy by Gene Silencing," *Biomaterials* 78 (2016): 27–39.

18. G. Xiao, Y. Zhao, X. Wang, C. Zeng, F. Luo, and J. Jing, "Photothermally Sensitive Gold Nanocage Augments the Antitumor Efficiency of Immune Checkpoint Blockade in Immune "Cold" Tumors," *Frontiers in Immunology* 14 (2023): 1.

19. E. Moysan, G. Bastiat, and J.-P. Benoit, "Gemcitabine versus Modified Gemcitabine: A Review of Several Promising Chemical Modifications," *Molecular Pharmaceutics* 10 (2013): 430–444, https://doi.org/10.1021/mp300370t.

20. H. Miao, X. Chen, and Y. Luan, "Small Molecular Gemcitabine Prodrugs for Cancer Therapy," *Current Medicinal Chemistry* 27 (2020): 5562–5582, https://doi.org/10.2174/0929867326666190816230650.

21. X. Zeng, L. Sun, X. Ling, et al., "Comprehensive Analysis Identifies Novel Targets of Gemcitabine to Improve Chemotherapy Treatment Strategies for Colorectal Cancer," *Frontiers in Endocrinology* 14 (2023): 1170526, https://doi.org/10.3389/fendo.2023.1170526.

22. C. Bornmann, R. Graeser, N. Esser, et al., "A New Liposomal Formulation of Gemcitabine is Active in an Orthotopic Mouse Model of Pancreatic Cancer Accessible to Bioluminescence Imaging," *Cancer Chemotherapy and Pharmacology* 61 (2008): 395–405, https://doi.org/10.1007/s00280-007-0482-z.

23. D. K. Kirui, C. Celia, R. Molinaro, et al., "Mild Hyperthermia Enhances Transport of Liposomal Gemcitabine and Improves in Vivo Therapeutic Response," *Advanced Healthcare Materials* 4 (2015): 1092–1103, https://doi.org/10.1002/adhm.201400738.

24. A. S. De Silva Indrasekara, S. F. Johnson, R. A. Odion, and T. Vo-Dinh, "Manipulation of the Geometry and Modulation of the Optical Response of Surfactant-Free Gold Nanostars: A Systematic Bottom-Up Synthesis," *ACS Omega* 3 (2018): 2202–2210, https://doi.org/10.1021/acsomega.7b01700.

25. S. Atta, M. Beetz, and L. Fabris, "Understanding the Role of $AgNO_3$ Concentration and Seed Morphology in the Achievement of Tunable Shape Control in Gold Nanostars," *Nanoscale* 11 (2019): 2946–2958, https://doi.org/10.1039/C8NR07615D.

26. N. T. Le, T. J. M. Boskovic, M. M. Allard, K. E. Nick, S. R. Kwon, and C. C. Perry, "Gold Nanostar Characterization by Nanoparticle Tracking Analysis," *ACS Omega* 7 (2022): 44677–44688, https://doi.org/10.1021/acsomega.2c03275.

27. A. P. Sangnier, R. Aufaure, S. Cheong, et al., "Raspberry-Like Small Multicore Gold Nanostructures for Efficient Photothermal Conversion in

the First and Second Near-Infrared Windows," *Chemical Communications* 55 (2019): 4055–4058, https://doi.org/10.1039/C8CC09476D.

28. B.-K. Jung, Y. K. Lee, J. Hong, H. Ghandehari, and C.-O. Yun, "Mild Hyperthermia Induced by Gold Nanorod-Mediated Plasmonic Photothermal Therapy Enhances Transduction and Replication of Oncolytic Adenoviral Gene Delivery," *ACS Nano* 10 (2016): 10533–10543, https://doi.org/10.1021/acsnano.6b06530.

29. A. Espinosa, A. K. A. Silva, A. Sánchez-Iglesias, et al., "Cancer Cell Internalization of Gold Nanostars Impacts Their Photothermal Efficiency In Vitro and In Vivo: Toward a Plasmonic Thermal Fingerprint in Tumoral Environment," *Advanced Healthcare Materials* 5 (2016): 1040–1048, https://doi.org/10.1002/adhm.201501035.

30. S. C. Freitas, J. H. Belo, A. Granja, et al., "Key Parameters in Phototherapy with Gold Nanorods Using Continuous Near Infrared Radiation," *Advanced Materials Interfaces* 10 (2023): 2202214, https://doi.org/10.1002/admi.202202214.

31. M. Boksebeld, V. Kilin, R. Taitt, et al., "Nonlinear Plasmonic Nanohybrids as Probes for Multimodal Cell Imaging and Potential Phototherapeutic Agents," *Biomedical Physics & Engineering Express* 5 (2019): 025039, https://doi.org/10.1088/2057-1976/ab0232.

32. J. He, S. Unser, I. Bruzas, et al., "The Facile Removal of CTAB from the Surface of Gold Nanorods," *Colloids and Surfaces B: Biointerfaces* 163 (2018): 140–145, https://doi.org/10.1016/j.colsurfb.2017.12.019.

33. M. Sahu, V. Reddy, M. Reddy, et al., "Fabrication of Cu_2ZnSnS_4 Light Absorber Using a Cost-Effective Mechanochemical Method for Photovoltaic Applications," *Materials* 15 (2022): 1708, https://doi.org/10.3390/ma15051708.

34. R. Gupta and D. Sharma, "Therapeutic Response Differences Between 2D and 3D Tumor Models of Magnetic Hyperthermia," *Nanoscale Advances* 3 (2021): 3663–3680, https://doi.org/10.1039/D1NA00224D.

35. A. Virgone-Carlotta, M. Lemasson, H. C. Mertani, et al., "In-Depth Phenotypic Characterization of Multicellular Tumor Spheroids: Effects of 5-Fluorouracil," *PLoS ONE* 12 (2019): 0188100, https://doi.org/10.1371/journal.pone.0188100.

36. P. Bregigeon, C. Rivière, L. Franqueville, C. Vollaire, J. Marchalot, and M. Frénéa-Robin, "Integrated Platform for Culture, Observation, and Parallelized Electroporation of Spheroids," *Lab on a Chip* 22 (2022): 2489–2501, https://doi.org/10.1039/D2LC00074A.

37. A. D. Hollander, G. Vande Velde, H. Jans, et al., "Assessment of the Theranostic Potential of Gold Nanostars—A Multimodal Imaging and Photothermal Treatment Study," *Nanomaterials* 10 (2020): 2112.

38. A. E. Nel, L. Mädler, D. Velegol, et al., "Understanding Biophysicochemical Interactions at the Nano–Bio Interface," *Nature Materials* 8 (2009): 543–557, https://doi.org/10.1038/nmat2442.

39. E. Darrigues, Z. A. Nima, D. A. Nedosekin, F. Watanabe, K. M. Alghazali, and V. P. Zharov, "Tracking Gold Nanorods′ Interaction With Large 3D Pancreatic-Stromal Tumor Spheroids by Multimodal Imaging: Fluorescence, Photoacoustic, and Photothermal Microscopies," *Scientific Reports* 10 (2020): 3362, https://doi.org/10.1038/s41598-020-59226-6.

40. E. C. Dreaden, L. A. Austin, M. A. Mackey, and M. A. El-Sayed, "Size Matters: Gold Nanoparticles in Targeted Cancer Drug Delivery," *Therapeutic Delivery* 3 (2012): 457–478, https://doi.org/10.4155/tde.12.21.

41. M. Kumar, P. Kulkarni, S. Liu, N. Chemuturi, and D. K. Shah, "Nanoparticle Biodistribution Coefficients: A Quantitative Approach for Understanding the Tissue Distribution of Nanoparticles," *Advanced Drug Delivery Reviews* 194 (2023): 114708, https://doi.org/10.1016/j.addr.2023.114708.

42. M. Yu and J. Zheng, "Clearance Pathways and Tumor Targeting of Imaging Nanoparticles," *ACS Nano* 9 (2015): 6655–6674, https://doi.org/10.1021/acsnano.5b01320.

43. W. Chen, D.-Y. Chang, B.-M. Chen, Y. Lin, Y. Barenholz, and S. R. Roffler, "Antibodies against Poly(ethylene glycol) Activate Innate Immune Cells and Induce Hypersensitivity Reactions to PEGylated Nanomedicines," *ACS Nano* 17 (2023): 5757–5772, https://doi.org/10.1021/acsnano.2c12193.

Supporting Information

Additional supporting information can be found online in the Supporting Information section.

Supporting File: ppsc70091-sup-0001-SuppMat.docx.